Journal of Manufacturing Processes
Vol. 3/No. 2
2001

Microscale Laser Shock Processing—Modeling, Testing, and Microstructure Characterization

Wenwu Zhang* and **Y. Lawrence Yao,** Dept. of Mechanical Engineering, Columbia University, New York, New York, USA

Abstract

This paper reports modeling improvements for microscale laser shock processing (LSP), fatigue testing of laser shock processed copper and nickel, and microstructure characterization of the processed materials. Plasma expansion is modeled as laser-supported combustion wave, and radial and axial expansions are considered. Stress/strain analysis is extended to three dimensions and takes into account finite geometry, which again is important for microscale LSP. Tests are designed to demonstrate that microscale LSP can improve fatigue performance of the materials while offering a level of flexibility. The influence of LSP on the microstructures of the materials is studied quantitatively using the orientation imaging microscope (OIM) technique, and grain size, texture, and subgrain structures are analyzed.

Keywords: *Microscale Laser Shock Processing, Laser-Supported Combustion Wave, Orientation Imaging Microscope (OIM), Stress/Strain Analysis, Fatigue*

1. Introduction

The expanding applications of micro devices make the mechanical properties of such devices an increasing concern. Processes that can improve the mechanical properties at microscale are required. Laser Shock Processing (LSP) at the millimeter scale (i.e., the focused laser beam diameter in the order of millimeters) has been used to improve the hardness, residual stress distributions, and thus fatigue life of metals (Claurer et al. 1981, Peyre et al. 1995, Berthe et al. 1998). More recently, laser shock processing of aluminum and copper at microscale has been studied (Zhang and Yao 2000a,b). It has been shown that it is possible to impart compressive residual stress tens of microns deep into target materials using a laser beam of a diameter of a few microns. The reduced scale requires reconsideration of a number of issues.

Previous shock pressure models assumed that a certain amount of plasma exists instantaneously once the laser is on (Claurer et al. 1981, Fabbro et al. 1990, Zhang and Yao 2000a,b). A constant fraction of plasma internal energy α was assumed to increase the pressure of the plasma. The way in which α was experimentally determined is rather cumbersome and indirect, and therefore most literature reported a constant value for different laser intensities. This value also varied from 0.1 to 0.4 across different literature. The reason is that in previous models there was no consideration of mass exchanges between plasma and confining medium (e.g., water) or plasma and target—only energy and momentum conservation were considered. Explicit consideration of the mass transfer in the model will eliminate the need for prescribing the value of α and thus reduce the arbitrariness and increase the model accuracy, which is crucial for the microscale under consideration.

The dynamic deformation process of the target material under the action of shock load had been simulated using the finite element method (FEM), but only for the one-dimensional case (Claurer et al. 1981, Peyre et al. 1995, Berthe et al. 1998) and the axisymmetric case (Zhang and Yao 2000a,b) where semi-infinity boundary conditions were implicitly assumed. Effects of finite size and complex geometry on shocking results were neglected when, in fact, they are very important in practice, especially for LSP of small components and LSP near edges of components.

LSP-induced compressive residual stresses deter crack initiation and propagation. As a result, fatigue life of shock-processed samples improved (Claurer et al. 1981, Zhang and Yu 1998). Comparable study of microscale LSP was not available. Microscale LSP can selectively treat a complex geometry with micron spatial resolution. The experimental condition of microscale LSP is very different from mil-

---

* Currently with General Electric Corporation R&D. E-mail: *wenwu.zhang@crd.ge.com*

limeter-scale LSP. The fatigue mechanism of microscale LSP requires further investigation.

Mechanical properties of shocked materials are closely related to their microstructures, including subgrain structures. The microstructure change in LSP was primarily studied using transmission electron microscopy (TEM) in the past, where increases of twinning and dislocation structures were reported (Murr 1981). Statistical and quantitative analysis of microstructure, especially subgrain structure change, accompanying LSP is desired but is inherently difficult using TEM.

In this paper, the expansion of plasma is modeled as 1D laser-supported combustion (LSC) wave. The 1D results are then modified to consider spatial expansion effects of the shock pressure. Copper and nickel samples are processed using microscale LSP and are compared with raw materials in terms of fatigue performance. 3D simulations of the shock-induced deformation process are carried out, where the effects of finite sample size and irregular geometry are considered. The Orientation Imaging Microscope (OIM) techniques are used to quantitatively and statistically characterize the microstructures and especially the subgrain structures of laser shock processed samples.

2. Modeling of Laser-Induced Shock Waves

As illustrated in *Figure 1a*, when a short and intense laser pulse is irradiated onto a coated metallic target, the coating instantaneously vaporizes into a high-temperature and high-pressure plasma. This plasma induces shock waves during expansion from the irradiated surface, and mechanical impulses are transferred to the target. If it is confined by a liquid (e.g., water) or another type of medium, the shock pressure can be magnified by a factor of 5 or more compared with the open-air condition (Fox 1974). The coating also protects the target from thermal effects so that nearly pure mechanical effects are induced.

Under typical conditions of LSP, the speed of plasma expansion is lower than the shock speed, thus the shock wave precedes plasma expansion. This resembles the case of a laser-supported combustion (LSC) wave (Root 1989). LSC wave in air and vacuum has been studied (Pirri et al. 1978) and will be extended in this paper to LSP modeling.

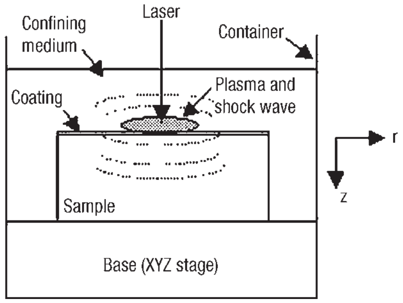

(a) Schematic of LSP

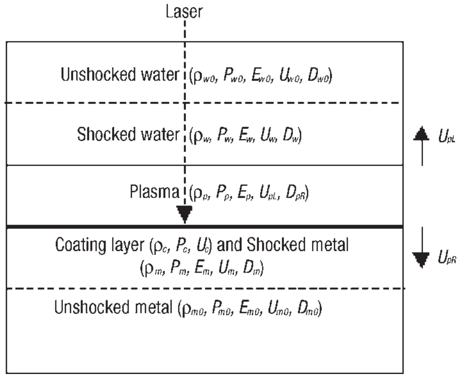

(b) Five regions in water-confined LSP

Figure 1
Laser Shock Processing (LSP)

Water is transparent to the laser beam if the laser intensity is below the breakdown level at the wavelength used. Water converts into plasma due to plasma and laser-induced water breakdown (Vogel et al. 1996). For UV lasers at $\lambda = 355$ nm, the breakdown level is around 4 GW/cm^2 (Berthe et al. 1998). In LSP, laser irradiation first vaporizes the surface layer of the coating, and the vaporized material quickly evolves into plasma. The plasma irradiation is primarily in the extreme ultraviolet (Root et al. 1979). At such short wavelengths (< 200 nm), multiphoton ionization (MPI) mechanism of water breakdown is dominant. Water near the plasma outer edge is quickly ionized and becomes strongly absorbent to incident laser irradiation. Thus, water is changed into plasma due to plasma irradiation and direct laser irradiation. At the same time, the coating is continuously vaporized into the plasma. The pressure of the plasma increases quickly and the expansion of the plasma imparts shock pressure into water and target. Mass, momentum, and energy are conserved across the shock wave. To model the process, the following assumptions are made.

(1) The early stage of plasma expansion is one dimensional; that is, plasma expands only in the axial direction. Density, internal energy, and pressure of the plasma are uniform within the plasma volume but can vary with time. Particle velocity of the plasma changes linearly from the water-plasma interface to the plasma-solid interface.
(2) Plasma obeys ideal gas laws.
(3) Only the coating layer is vaporized; the metal target experiences negligible thermal effects. The melting layer, Knudsen layer, and the transition region from vapor to plasma of the coating layer are so thin that their thickness is negligible compared with the thickness of plasma. Their influence can be represented by the phase-change energy in the energy conservation relation.
(4) The coating layer is thin and well coupled with the metal target; thus, the shock pressure and the particle velocity of the coating layer and the metal target are equal.

Let subscripts w denote water, m metal, c the coating layer, p plasma, L the side of plasma near water, R the side of plasma near solid, and 0 the property of unshocked region. Also, let D be shock velocity, U particle velocity, E internal energy, ρ density, and P pressure. For convenience, the water-plasma-target system is divided into five regions (*Figure 1b*): unshocked water (ρ_{w0}, P_{w0}, E_{w0}, U_{w0}, D_{w0}), shocked water (ρ_w, P_w, E_w, U_w, D_w), plasma (ρ_p, P_p, E_p, U_{pL}, U_{pR}), coating layer and shocked solid (ρ_c, P_c, U_c, ρ_m, P_m, E_m, U_m, D_m), and unshocked solid (ρ_{m0}, P_{m0}, E_{m0}, U_{m0}, D_{m0}). The unshocked properties are known. The shocked and unshocked properties of water are related by mass, momentum, and energy conservation, and shock speed constitutive relations:

$$\rho_{w0} / \rho_w = 1 - (U_w - U_{w0}) / (D_w - U_{w0}) \tag{1}$$

$$P_w - P_{w0} = \rho_{w0}(D_w - U_{w0})(U_w - U_{w0}) \tag{2}$$

$$(E_w + U_w^2/2) - (E_{w0} + U_{w0}^2/2) = \frac{1}{2}(P_w + P_{w0})\left(\frac{1}{\rho_{w0}} - \frac{1}{\rho_w}\right) \tag{3}$$

$$D_w = D_{w0} + S_w U_w \tag{4}$$

For water, $U_{w0} = 0$ m/s, $P_{w0} = 10^5$ Pa, $E_{w0} = 0$ J/kg, $\rho_{w0} = 997.9$ kg/m^3, $D_{w0} = 2393$ m/s, and $S_w = 1.333$ (Assay and Shahinpoor 1992). S_w is a coefficient relating shock speed D_w to U_w, the particle velocity, and D_{w0}, the shock speed at infinitesimally small particle velocity.

Substituting subscript m for w in Eqs. (1) to (4), one obtains four more equations between shocked and unshocked properties of metals. $U_{m0} = 0$ m/s, $P_{m0} = 10^5$ Pa, and $E_{m0} = 0$ J/kg. For copper, $\rho_{m0} = 8939$ kg/m^3, $D_{m0} = 3933$ m/s, and $S_m = 1.489$. For nickel, $\rho_{m0} = 8874$ kg/m^3, $D_{m0} = 4581$ m/s, and $S_m = 1.463$ (Meyers and Murr 1981).

The above equations can be solved after considering their interactions with the plasma. Mass and momentum conservation at the interfaces at any instant requires:

$$\rho_w(U_{pL} - U_w) = \rho_p U_{pL} \tag{5}$$

$$\rho_c(U_{pR} - U_c) = \rho_c Vrec = \rho_p U_{pR} \tag{6}$$

$$P_p + \rho_p U_{pR} U_c = P_c \tag{7}$$

$$P_p + \rho_p U_{pR} U_w = P_w \tag{8}$$

The current mass of the plasma is equal to the integration of the mass flows into plasma. The mass flow from water is $MF_w = \rho_w (U_{pL} - U_w)$. The mass flow from the coating layer is $MF_c = \rho_c (U_{pR} - U_c) = \rho_c Vrec$, where $Vrec$ is the recess velocity of the melting coat surface. In this paper, the coating layer is aluminum foil, $\rho_c = 2700$ kg/m^3. According to assumption (4), $U_m = U_c$ and $P_m = P_c$. The mass conservation of plasma requires:

$$\rho_p(t)\int_0^t (U_{pL} + U_{pR})dt = \int_0^t (MF_w + MF_c)dt \tag{9}$$

The energy conservation of plasma should consider the absorption of incident laser irradiation, the total energy stored in the plasma, the work done by the plasma, and energy exchanges through mass flow. The total energy consists of kinetic energy and internal energy. Based on the assumption of linear distribution of particle velocity, the unit mass kinetic energy of plasma is $E_{pk} = (U_{pL}^2 + U_{pR}^2 - U_{pL}U_{pR})/6$. Using the ideal gas law, the internal energy of plasma is related to its density, specific heat ratio γ (about 1.3), and pressure:

$$E_p = \frac{\gamma P_p}{(\gamma - 1)\rho_p} \tag{10}$$

So the total energy in plasma is $E_{pt} = \rho_p L\,(E_{pk} + E_p)$, where $L(t) = \int_0^t \left(U_{pL} + U_{pR}\right)dt$ is the plasma length. The total work done by plasma to the surrounding is $W_p = \int_0^t P_p\left(U_{pL} + U_{pR}\right)dt$. The mass exchange induced energy exchange equals mass flow times the energy difference:

$$E_{MF} = \int_0^t \Big[MF_c\left(E_{pk} + E_p - U_c^2/2 - Q_c\right) + MF_w\left(E_{pk} + E_p - U_w^2/2 - Q_w\right)\Big]dt$$

where Q_w and Q_c are the phase-change energy of water and coating layer, respectively. The internal energy is incorporated in the phase energy term.

Let AP be the fraction of laser energy absorbed by plasma, and $I(t)$ the laser intensity, the energy conservation of plasma, requires:

$$E_{pt} + W_p - E_{MF} = \int_0^t AP \times I(t)\,dt \tag{11}$$

AP can be decided from experiments. Now the equations of this 1D model are closed and all the variables involved can be solved as a function of time.

Radial expansion of plasma is a more significant concern in microscale LSP than in millimeter-scale LSP because such expansion may not be neglected because of the small beam size. Once plasma is created, radial expansion of plasma commences. A rarefaction wave propagates into the plasma from the edge at the sound speed of the plasma. After a characteristic time $T_r = R_0/a$, where R_0 is the radius of the laser beam and a is the sound speed of the plasma, the rarefaction wave coalesces at the center of the spot. The pressure of the plasma drops and deviates from the 1D values afterward. Axial relaxation starts after the laser pulse terminates; thus, the characteristic time for axial expansion is $T_z = T_p$, where T_p is pulse duration. The temporal evolution of the plasma depends on the values of T_r and T_z. For the laser used in current research, $R_0 = 6$ microns, $T_z = T_p = 50$ ns, and sound speed of plasma $a = 300$ m/s, $T_r = 20$ ns; thus, radial relaxation occurs earlier than axial relaxation. Based on the work of Pirri (1978), Simons (1984), and Root (1989), the following power scaling laws are used in this paper.

$$t < T_r \qquad \begin{aligned} P &= P_{1D} \\ R &= R_0 \end{aligned}$$

$$T_z > t > T_r \qquad \begin{aligned} P &= P_{1D}\left(t / T_r\right)^{-4/5} \\ R &= R_0\left(t / T_r\right)^{1/2} \end{aligned} \tag{12}$$

$$t > T_z \qquad \begin{aligned} P &= P_{1D}\left(T_r / T_z\right)^{4/5}\left(T_z / t\right)^{6/5} \\ R &= R_0\left(T_z / T_r\right)^{1/2}\left(T_z / t\right)^{-4/5} \end{aligned}$$

where P_{1D} is the plasma pressure from the 1D model described above.

For laser shock processing on micron scale, the spatial profile of the laser beam should also be considered. Following the work of Zhang and Yao (2000a), shock pressure obeys Gaussian spatial distribution, but with its $1/e^2$ radius equal to $\sqrt{2}R(t)$, where $R(t)$ is the radius of plasma in Eq. (12). Letting r be the radial distance from the center of the laser beam, the spatially uniform shock pressure $P(t)$ relates to the spatially nonuniform shock pressure as

$$P(r,t) = P(t)\exp\left(-\frac{r^2}{2R^2(t)}\right) \tag{13}$$

3. Experimental and Simulation Conditions

3.1 Selection of Materials and Experimental Conditions

Microscale LSP can be applied to a variety of metals. Copper and nickel are chosen in this study because they are often etched and deposited on silicon substrates as part of micro devices. Nickel is also used as a metallic MEMS material. The mechanical properties of nickel and copper are different. For instance, the Young's modulus of copper and nickel are 120 and 220 GPa, respectively. The ultimate strengths of annealed copper and nickel are 215 and 400 MPa, respectively.

Response of material to shock wave is described by Hugniot relations [Eqs. (1) to (4)]. Specifying any one of the five unknowns (shock pressure, particle velocity, shock velocity, density, or internal energy), the other four can be expressed as a function thereof. Study of the Hugniot curves of nickel and copper shows that nickel has obviously smaller variation of density and particle velocity than copper for the same shock pressure. For example, *Figure 2a* compares the density of copper with nickel as a

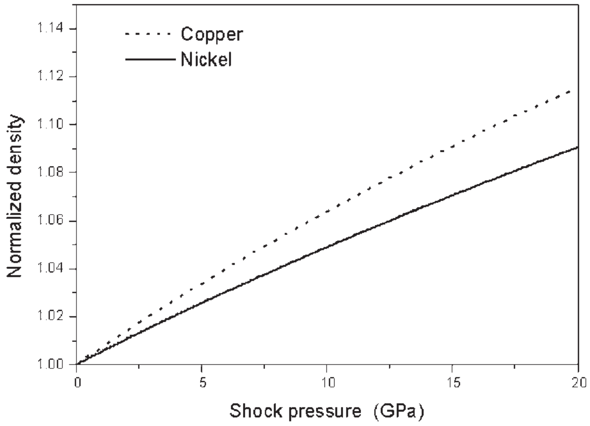

(a) Variation of normalized density (ρ/ρ_0) with shock pressure

(b) Influence of strain rate and shock pressure on yield strength of Cu and Ni

Figure 2
Property Comparisons of Nickel and Copper

function of shock pressure. The density is normalized against the density under one atmosphere pressure, ρ_0. At the shock front, metal is compressed and its density increases. As seen, the increase of the normalized density of nickel with shock pressure is about 20% less than that of copper.

The influences of strain rate and shock pressure on the yield strength of copper and nickel are compared in *Figure 2b* based on the constitutive equations (Zhang and Yao 2000a). For copper, the influence of strain rate is larger than but comparable with the influence of shock pressure, while the increase of yield stress of nickel with strain rate is only half the increase with shock pressure. In general, nickel is less sensitive to shock pressure and strain rate than copper is. The increase of yield strength of copper with strain rate is six times that of nickel, and twice that of nickel with shock pressure.

Copper foils of 90 micron thickness and nickel foils of 120 micron thickness were used in LSP experiments. The samples were adhesively attached to bulk copper columns for rigid support and easy handling. The samples were polished, and the sample size was about 8 mm square. To apply the coating, a thin layer of high-vacuum grease (about 10 microns) was spread evenly on the polished sample surface, and the coating material, aluminum foil of 25 microns thick, which was chosen for its relatively low threshold of vaporization, is then tightly pressed onto the grease. The sample was placed in a shallow container filled with distilled water around 3 mm above the sample. A frequency-tripled Q-switched Nd:YAG laser in TEM_{00} mode was used, the pulse duration was 50 ns, and pulse repetition rate could vary between 1 kHz to 20 kHz. Laser beam diameter was 12 microns. After shock processing, the coating layer and the vacuum grease were manually removed. The pulse number at each location was varied from 1 to 6 at 1 kHz repetition rate, and pulse energy was varied from 160 μJ to 240 μJ corresponding to laser intensity of 2.83 to 4.24 GW/cm^2. LSP at individual locations (similar to drilling) and overlapped locations (similar to grooving) was carried out.

The geometry of the shocked region was observed and measured using optical microscopy, scanning electron microscopy (SEM), and interferometry-based optical profilometry. Fatigue tests of unshocked and shocked samples were carried out using a material testing system. orientation imaging microscopy (OIM) measurements of microstructures and especially subgrain structures were carried out. More details of these measurements are described in the corresponding sections of results and discussion.

3.2 Simulation Conditions

The spatial and temporal-dependent shock pressure was solved numerically based on what was outlined in section 2 and used as the loading for the subsequent stress/strain analysis. In the stress/strain analysis, work hardening, strain rate, and pressure effects on yield strength are considered (Zhang and Yao 2000a) assuming room temperature. This is reasonable because only the coating is vaporized and minimal thermal effects are felt by the sample. A commercial FEM code, ABAQUS, is used for the stress/strain analysis as a dynamic implicit nonlinear process. First, axisymmetric modeling was carried out to compare the effects of the current shock pressure model with the previous model on deformation (Zhang and Yao 2000a) assuming semi-infinity in geometry. Single and multiple pulses at individual locations were simulated. Secondly, 3D simulation was carried out assuming finite geometry (100 microns thickness, 1 mm width, and 2 mm length). Pulses at overlapped locations with 50 micron spacing were simulated. Shocks are applied on the top surface along a narrow strip in the width direction. The bottom surface is fixed in position, while all the other side surfaces are set traction free. The 3D simulations were extended to consider the specimen geometry used in the fatigue tests. The geometry and finite size effects were studied to explain the fatigue test results.

4. Results and Discussion

4.1 Results of Shock Pressure Modeling

In previous modeling work, mass flow from water into plasma and from target into plasma along with the property changes of water, target, and plasma, are neglected (Fabbro et al. 1990, Zhang and Yao 2000a). Plasma grows as the target material and water break down into plasma. The evolution of mass flow from water into plasma is shown in *Figure 3a*, which also shows the laser intensity profile normalized to the peak intensity. It is observed that the mass flow peaks after laser intensity peaks. The reason is that mass flow from water into plasma is caused by water breakdown, which in turn is due to the combined effects of laser and plasma irradia-tion. Even after the laser intensity peaks, the plasma irradiation sustains the mass flow for a period of time. As laser intensity increases, plasma accumu-lates more energy to irradiate. This is why it takes longer for the mass flow to peak when laser intensity increases. The mass flow from the coating layer into plasma has similar features and is about one order of magnitude lower than the mass flow from water into plasma. These mass flows contribute to the evolution of plasma and the expansion of plasma imparts high shock pressures into water and the target solid.

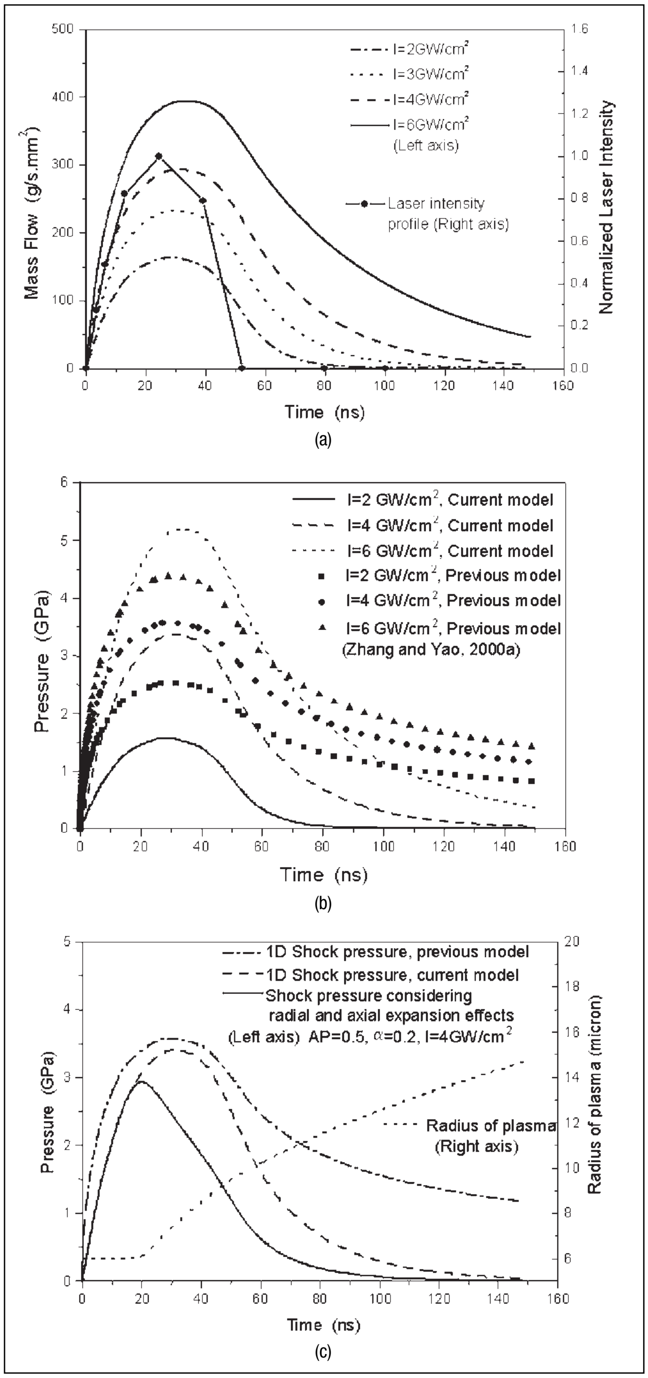

Figure 3
(a) Mass flow from water into plasma and normalized profile of laser intensity; (b) 1D shock pressure comparison of current model and previous model (Zhang and Yao 2000a); and (c) Consideration of radial and axial expansion effects

Figure 3b compares the 1D shock pressure determined using the current model and the previous model (Zhang and Yao 2000a). The previous model assumed that a constant fraction $\alpha = 0.2$ of plasma energy is used to increase the shock pressure during

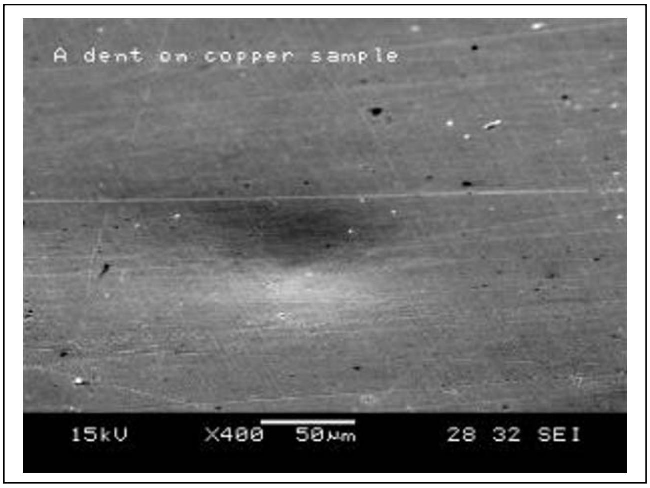

Figure 4
Dented Area Made by LSP on Copper Foil, E = 220 μJ, three pulses. Note the dent is due to shock pressure not thermal effects because only coating is vaporized and therefore is a clear indication of plastic deformation (SEM taken at the 60 degree angle)

the expansion of the plasma. In the current model, such conversion is inherently considered in the energy balance relations. As seen, the previous model determined a higher peak pressure at laser intensity of 2 GW/cm², a comparable value at 4 GW/cm², and a lower value at 6 GW/cm² than the current model. This is indicative of the shortcoming of using a constant value of α for different laser intensities in the previous model. As the energy level increases, the plasma tends to expand faster but experiences a higher level of resistance by water. As a result, the plasma spends a larger fraction of its internal energy on pressure increases and thus a larger value of α should have been used to account for this effect. The pressures recover to zero values faster in the current model than in the previous model. The reason is that in the current model, plasma energy is used for the breakdown of water and the target material besides the expansion of plasma, while in the previous model only the 1D expansion of plasma was considered.

For laser beam size of micron scale, the radial and axial expansion effects on plasma must be accounted for. Equation (13) was used to calculate the final shock load used in stress analysis. The temporal evolution of shock pressure and the radius of plasma at laser intensity of 4 GW/cm² are shown in *Figure 3c*. The radius of plasma is constant until the rarefaction wave merges at the center of the laser beam at about 20 ns. After that, a nonlinear increase of plasma radius occurs. The shock pressure decreases after the rarefaction wave merges at the beam center according to power laws showed in Eq. (12). Obviously the shock pressure considering plasma expansion is more realistic and more suited for microscale LSP.

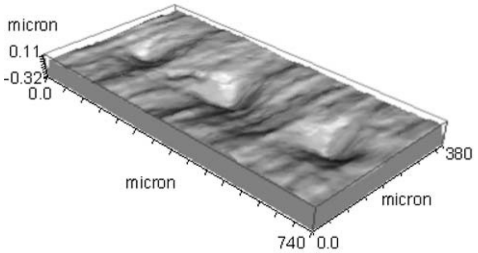

(a) Dents on nickel sample, E=220μJ, four pulses

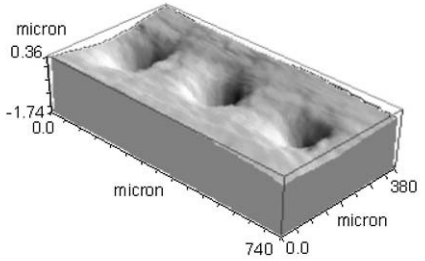

(b) Dents on copper sample, E=220μJ, four pulses

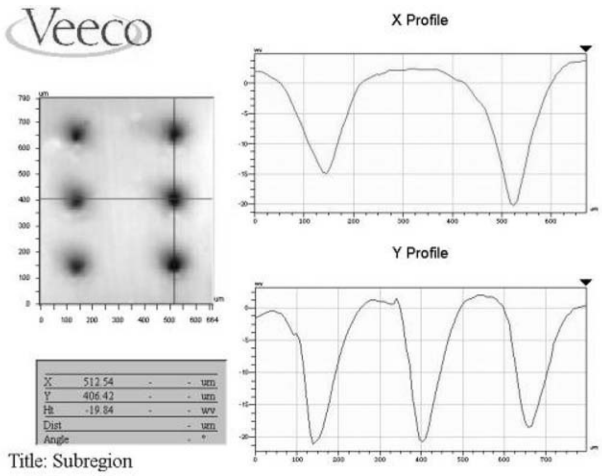

X	512.54	-	-	um
Y	406.42	-	-	um
Ht	-19.84	-	-	wv
Dist			-	um
Angle			-	°

Title: Subregion

(c) Measurement of cross section (in vertical direction 1 wv = 0.1 micron)

Figure 5
Measurement of Dent Geometry Using Optical Profilometry

4.2 Deformation and Model Validation

Figure 4 shows a dent on a copper sample induced by three laser pulses with pulse energy 220 μJ (3.89 GW/cm²). Note the dent is due to shock pressure and not due to thermal effects because only the coating is vaporized. The dent is a clear indication of plastic deformation. The dent is smooth and round with radius of about 50 microns (the focused

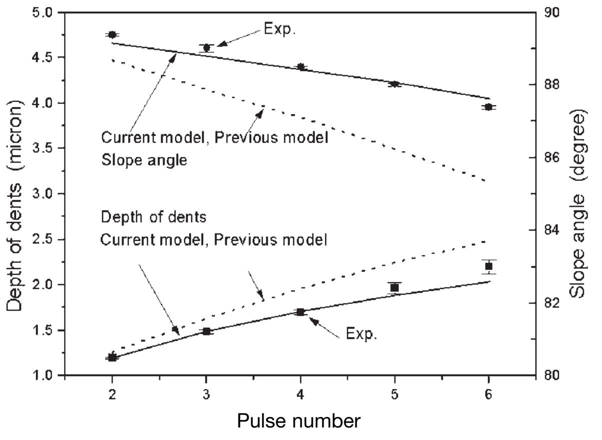

(a)

(b)

Figure 6
Dent Geometry Comparisons Between Current Model and Previous Shock Pressure Model. For stress/strain analysis of the simulation, refer to Zhang and Yao (2000a). (a) Copper and (b) Nickel. E=220 μJ, I=3.89 GW/cm^2

laser beam diameter is 12 microns). To quantitatively characterize the deformation, an interferometry-based optical profilometer with a vertical resolution of 3 nm is used to profile deformed regions under this and other conditions. *Figures 5a* and *5b* show the 3D plots of dents on nickel and copper samples under the condition of E = 220 μJ and four pulses. The dent depth of copper is about 2 microns, the dent depth for nickel is only about 0.4 microns, while the dent diameter is rather close for both materials. *Figure 5c* shows the cross-sectional measurements of the dents. The x-profile shows the cross section of two dents. The left dent is induced by four pulses, and the right dent is induced by five pulses. From such profiles, the depth and the slope angle of the dents are measured and compared with simulations. The slope angle is defined as the angle between the surface normal and the average tangential line of the dent slope.

Figures 6a and *6b* show the variation of dent depth and slope angle with the increase of pulse number at E = 220 μJ (3.89 GW/cm^2) for copper and nickel samples, respectively. Each experimental data point is the average of more than three features, and the error bar represents standard deviation. Simulation results of current and previous shock pressure model (Zhang and Yao 2000a) are also superposed. The stress/strain analysis of the simulation is the same as reported in Zhang and Yao (2000a).

The current model agrees well with the experimental results, while the previous model overestimates the dent depth especially at the larger number of pulses. This is primarily due to the fact that the previous model overestimated the shock pressure duration by neglecting the radial and axial expansions of the plasma (*Figure 3c*). When the number of pulses increases, the effect of such overestimation accumulates. This explains why the discrepancy gets larger with the number of pulses. The discrepancy in the slope angle can be similarly explained. Simulations and experiments under a wide range of other conditions showed similar trends.

4.3 Fatigue Performance Improvement Through Microscale LSP

It has been shown that millimeter-scale LSP can improve fatigue life of metals. It can typically induce plastic deformation up to 1 mm deep into target material and compressive residual stress up to -400 MPa (Clauer et al. 1981). Millimeter-scale LSP, however, requires the use of high-energy laser pulses, which limits the pulse repetition rate to as low as 2 shocks/minute (Berthe et al. 1998). Millimeter-scale LSP has a limited spatial resolution and is not suited for microscale device treatment. Lasers that are used in microscale LSP having much smaller beam sizes (12 microns in this paper) have two advantages. First, the laser delivers laser intensities comparable to that used in the millimeter-scale LSP but allows for a higher repetition rate (1 kHz or higher in this paper). More importantly, the smaller footprint of treatment made possible by the smaller beam size provides greater flexibility in treating

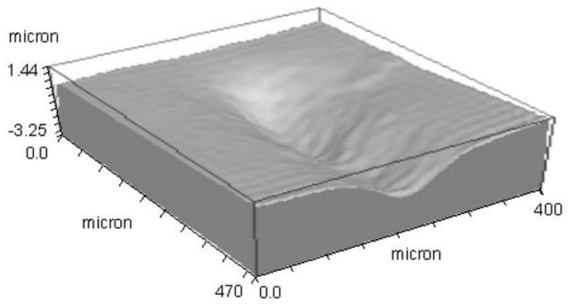

Figure 7
Optical Profilometer Measurement of Laser Shock Induced Deformation (Groove) on Copper (laser pulses were overlapped with 50 micron spacing, three pulses at each location, E=220 μJ)

smaller devices and devices with complex geometry. Microscale LSP can selectively treat critical regions such as regions around stress raisers on microscale devices at high speeds. Microscale LSP can be overlapped to treat large areas (*Figure 7*); at the same time, the geometry of the laser shocked area can be controlled with micron accuracy. Of course, the concern is whether microscale LSP will improve fatigue life as millimeter-scale LSP does. After all, the microscale LSP only imparts plastic deformation in the order of tens of microns deep and compressive residual stress about a half or an order of magnitude smaller than that induced by the millimeter-scale LSP (Zhang and Yao 2000b). It is the purpose of this section to investigate this issue.

The geometry of the fatigue test specimen is shown in *Figure 8a*. It is a scaled-down version of the standard tensile test specimen. The copper sample is 0.8 mm in thickness with two half-circle notches of radius of 0.5 mm to introduce stress concentration and more complex geometry effects. Microscale LSP is used to treat the dotted region between and around the notches, and both sides of the specimen are shock processed. Laser pulse energy is 220 μJ. Two, three, or four laser pulses at repetition rate of 1 kHz are applied at each location, and the shocked locations in the dotted region are spaced by 50 microns. The fatigue test was done on a material testing machine, and a 80 Hz sinusoidal load was applied axially. To prevent backlash, a positive mean load is applied such that the total load always oscillates in the tensile territory. It is mainly the tensile stress that is responsible for the initiation and propagation of cracks. Five pairs of tests were conducted covering the range from the fatigue strength to the ultimate strength of copper. *Figure 8b* compares the typical fatigue curves of identical specimens with LSP and without LSP. It is seen that the fatigue life of the specimen with LSP is about three times that of the specimen without LSP, noting the logarithmic scale used.

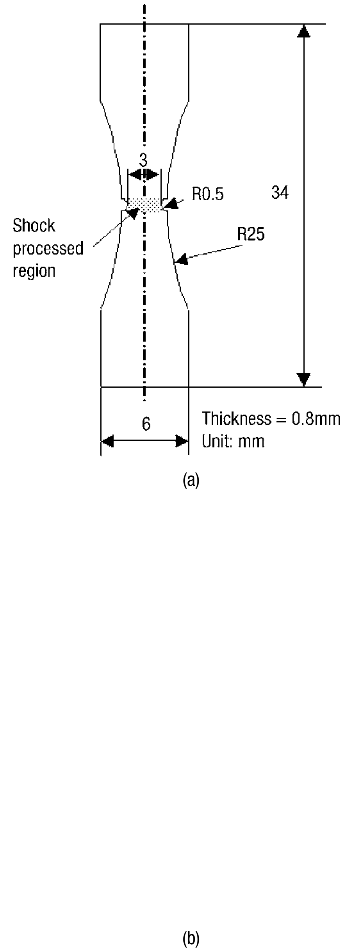

Figure 8
(a) Geometry of fatigue test sample and (b) Results of fatigue test. The dotted region near the notches is laser shock processed by scanning laser pulses along the width direction at a uniform spacing of 50 microns, three pulses at each location, pulse energy E=220 μJ. The lines in (b) are least-square fitted curves of the experimental results (note the logarithmic scale).

Although it is difficult to directly compare the fatigue test results of millimeter-scale LSP and microscale LSP due to different process conditions involved, microscale LSP can increase the fatigue life of metal components as millimeter-scale LSP does, but its high repetition rate and high spatial resolution make it more flexible for treating normal-sized samples, especially the ones with more complex geometry. More importantly, only the microscale LSP offers the capability to treat micro

Table 1
Fatigue Testing Results of Shock-Processed Copper Samples
(sinusoidal load frequency = 80 Hz, mean stress = 103.5 MPa, and stress oscillation amplitude = 95.5 MPa)

	Two Pulses	Three Pulses	Four Pulses
With LSP	60,873±730 cycles	76,845±610 cycles	53,458±692 cycles
Without LSP	25,506±588 cycles	25,506±588 cycles	25,506±588 cycles
With/Without Ratio	2.39±0.03	3.01±0.02	2.10±0.02

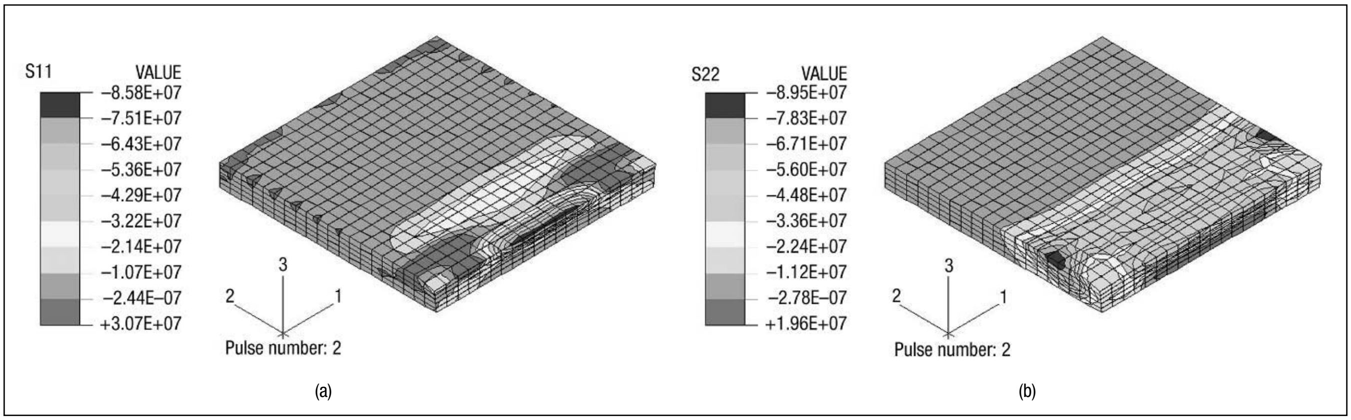

(a) (b)

Figure 9
Residual Stress Distribution of Laser Shock Processed Copper Plate. (a) S11 and (b) S22. A series of successive shocks (with spacing of 50 microns) is applied along the centerline (shown in dotted line) of the 1 mm by 2 mm by 0.1 mm copper plate. Only half the plate is shown due to symmetry. Two pulses at each location with pulse energy 220 µJ.

devices. It appears that the fatigue prevention mechanism does not differ significantly between the millimeter-scale LSP and microscale LSP.

Table 1 shows the influence of pulse numbers on the fatigue life of copper under one of the five testing conditions (mean stress = 103.5 MPa and stress oscillation amplitude = 95.5 MPa). Two, three, and four pulses were applied at each location, and each test was repeated three times. Contrary to intuition, the fatigue life deteriorated when more than three shock pulses were used, although the fatigue life is still much better than that without LSP. This phenomenon will be explained in conjunction with the 3D simulation results in section 4.4.

4.4 Three-dimensional Stress/Strain Analysis with Finite Geometry

Axisymmetric stress/strain analysis was conducted for microscale LSP at individual locations (Zhang and Yao 2000a,b), in which semi-infinite geometry was also assumed. Such analysis results are used in *Figure 6* to compare with experimental measurements. For LSP at overlapped locations, as in the case of fatigue specimen described in the last section, 3D stress/strain analysis will be necessary. In addition, for such geometry and for small-scale specimens, the semi-infinite geometry assumption needs to be removed. Such simulation helps examine the residual stress states and understand the fatigue performance. *Figures 9* and *10* show typical 3D stress/strain analysis results where finite geometry is considered.

Figures 9a and *9b* illustrate the residual stress distributions of S11 (along laser scanning direction) and S22 (vertical to laser scanning direction), respectively. Two observations can be made. First, the stress state at the edge areas is more complex than that in the interior area. This is obviously due to the effect of finite geometry. Typically, less resistance to deformation is experienced at the edge areas. The residual stress state at the edge areas has significant influence on crack initiation and propagation. Secondly, S22 is more uniformly distributed than S11. *Figure 9b* shows that LSP induced an area of surface compressive residual stresses perpendicular to the scanning direction, and the area extends 300 microns from the centerline. The maximum compressive stress is close to –90 MPa. If the specimen experiences a periodic load along the S22 direction, the surface compressive residual stress will help improve its fatigue life. In fact, the compressive stress extends into the depth direction, which will be further discussed when *Figure 10* is explained.

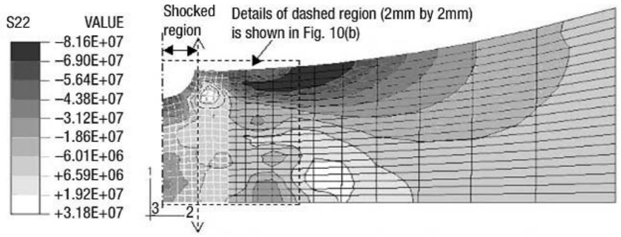

(a) Cu fatigue sample — three pulses

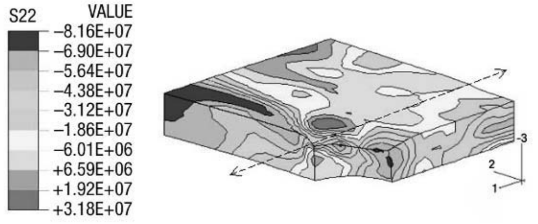

(b) Cu fatigue sample — three pulses

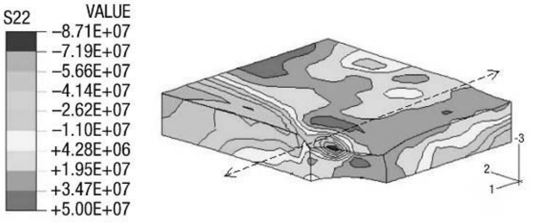

(c) Cu fatigue sample — four pulses

Figure 10
Residual Stress Distribution of Laser Shock Processed Fatigue Specimen. (a) Top view of specimen overlaid with S22 distribution, three pulses. The geometry is the same as that shown in *Figure 8a* but was scaled down by 50%. In addition, only 1/8 thereof is simulated due to symmetry (shocked on both sides). (b) Detailed view of notched region, three pulses. (c) Detailed view of notched region, four pulses. The volume shown in *Figures 10b* and *10c* is 2 mm in 1-1 direction, 2 mm in 2-2 direction, 0.2 in 3-3 direction. Notch radius is 0.5 mm. The dotted line shows the boundary of the laser shock processed region near the notch. LSP was carried out at a uniform spacing of 50 microns and pulse energy E=220 µJ. Note the deformation seen at the shock-processed region.

Figure 10a shows the geometry of the fatigue sample and the distribution of S22 on the top surface for three pulses. The simulation condition was similar to that used to process the fatigue specimen. S22 is compressive in the shocked region, including the notched area. A 2 mm by 2 mm region close to the notched area is shown in detail in *Figure 10b*. As seen, S22 is compressive around the notched area and throughout the depth direction, reaching a peak value of –80 MPa. Such compressive stress distribution is favorable for crack prevention and fatigue life improvement.

The distribution of S22 is similar to that of three pulses when two pulses were used, but the compressive stress level is lower (–57 MPa). When four pulses were used, S22 becomes partially tensile in the shocked region, as shown in *Figure 10c*. This counterintuitive change is due to overly large plastic deformations in the shocked region. Large downward (33 direction) pressure primarily causes excessive deformation in the outward (11 direction) in which least resistance is experienced. Based on the constant volume principle of plastic deformation, the stress in the 22 direction becomes slightly tensile. This explains why the fatigue specimen treated with four pulses at each location did not perform as well as that treated with two and three pulses (*Table 1*). More generally, this is indicative of the effects of shock processing conditions on residual stress distributions.

4.5 Microstructure Study of Laser Shock Processed Samples

The effects of LSP on the target material can be better understood through the study of its microstructures, which are responsible for its macroscopic properties. In the past, transmission electron microscopy (TEM) was used to study the dislocation density changes in high-pressure (up to 100 GPa) shock processing, and dislocation cell structures in shock-processed copper and nickel samples were observed (Meyers and Murr 1981). Dislocation densities in laser shock processed and unprocessed aluminum alloys were qualitatively compared by Clauer et al. (1981) using TEM. Other aspects of microstructure changes caused by LSP, including grain orientation and texture, have not been studied.

In this paper, orientation imaging microscopy (OIM) was used to study the microstructure changes quantitatively. In an OIM system, the Electron Back-Scatter Diffraction (EBSD) patterns are recorded, and the bands in these patterns are termed Kikuchi bands. Kikuchi bands are representative of lattice planes in the diffracting crystal. Such patterns are auto-indexed to extract the lattice orientation information. OIM has some special advantages in microstructure analysis over TEM. The sample preparation of OIM is not destructive, thus the nearly original state of the sample can be observed. A much larger area than TEM can be quantitatively and statistically analyzed. The OIM micrograph accurately reproduces the features visible in the optical micrograph, but contains inherently greater crystallographic details, and the spatial resolu-

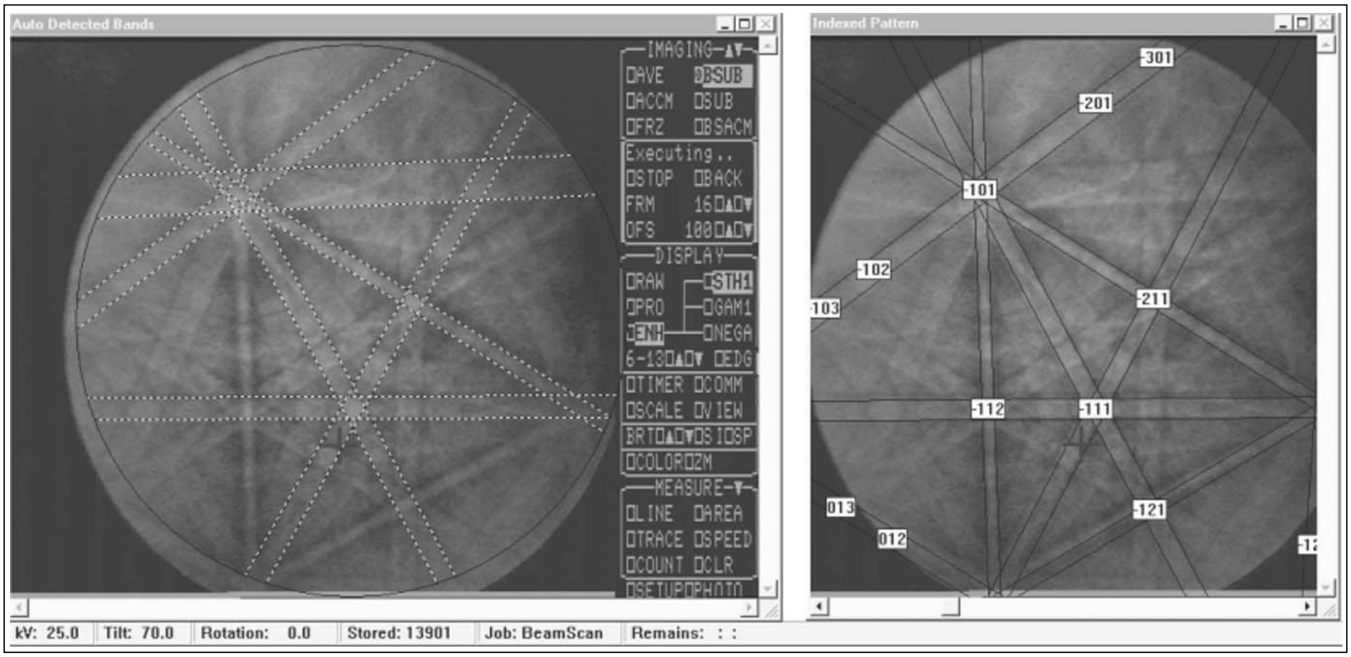

kV: 25.0 | Tilt: 70.0 | Rotation: 0.0 | Stored: 13901 | Job: BeamScan | Remains: : :

Figure 11
Illustration of OIM Measurement of Nickel Sample. Left window shows the auto-detected Kikuchi bands in the EBSD pattern of nickel; right window shows auto-indexing of the pattern.

tion can reach submicrons. OIM measurements of nickel and copper samples were carried out. A square region of the samples was shock processed (spacing of 50 microns, two pulses at each location, and pulse energy of 220 μJ). The samples were briefly chemical etched to remove the mechanical scratches on the surface. The shocked region was accurately located using SEM before the OIM measurements. The shocked region and shock-free region were compared.

Figure 11 shows the OIM measurement of nickel. The scanning step size is one micron and the grain size is over five microns. A rectangular region was scanned line by line. The region was chosen to cover enough number of grains for statistic purposes. The left window shows the Kikuchi bands in the EBSD pattern at the current scanning location. The right window shows the auto-indexing of the pattern. Through the indexing, the orientation of the lattice at the current location is determined. After a representative region of the sample was scanned, the statistics of the sample microstructures and lattice orientations were analyzed.

Grain size and uniformity. Grain boundaries were distinguished by defining the corresponding misorientation angles, and the grain size distribution of the sample was found using the OIM post-processing software. For instance, by setting misorientation angle of grain boundary to be 10 degrees, it was found that the grain size after microscale LSP did not change significantly, and this agrees with previous studies that found that grain sizes change significantly only when very high pressures are applied (Meyers and Murr 1981). The standard deviations of grain size, however, for both copper and nickel were reduced by more than 20% after LSP, which means the grains become more uniform after LSP. When the mean grain size is the same, the material with more uniform distribution of grain size has higher yield strength compared with the material with more scattered grain size distribution. The reason is that plastic strain is unevenly distributed among grains of different sizes (Novikov 1997). Uniform grain size tends to share the external load more uniformly and is desirable for neutralizing weak spots and thus stress concentration.

Crystallographic texture. Crystallographic texture refers to the preferred orientation, that is, the nonrandom orientation of individual crystal lattices within a material. Lattice orientation is defined by three Euler angles relative to the sample coordinates or laboratory (SEM chamber) coordinates. Misorientation angle between two points (or two directions) is defined as the minimum rotation angle needed to bring their lattice coordinates (or two directions) into coincidence. Pole figures or inverse pole figures are commonly used to analyze textures

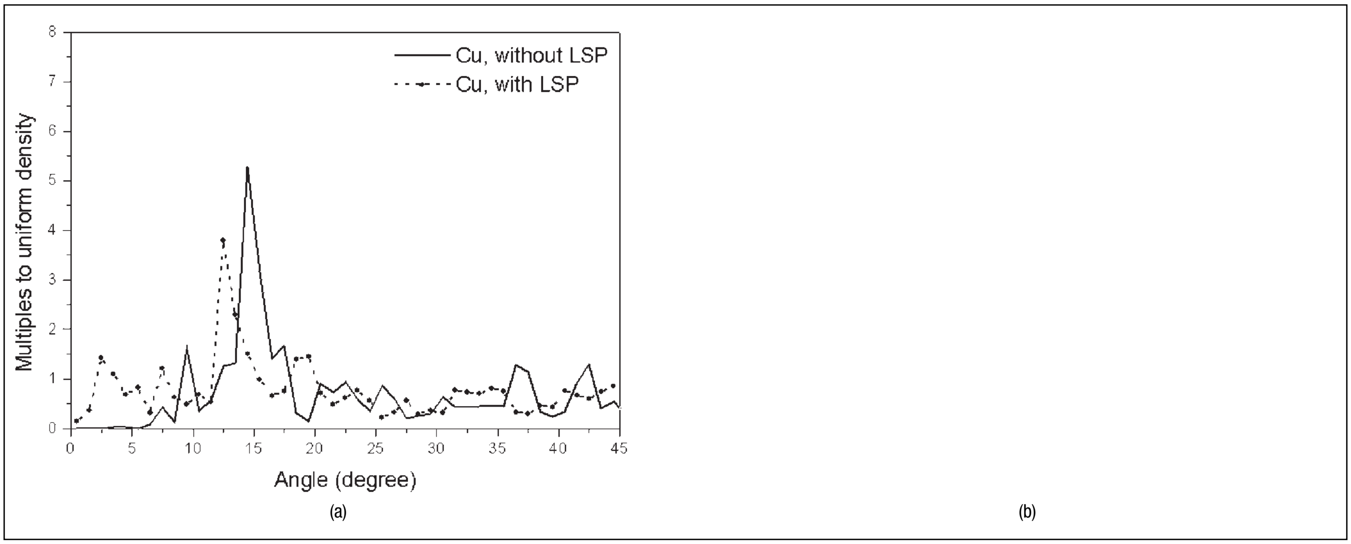

(a)

(b)

Figure 12
Misorientation Angle Distribution of {001} Lattice Direction. (a) Copper and (b) Nickel. The misorientation angle is the angle between {001} poles and the surface-normal direction of the sample. Vertical axis is the relative density compared with average density.

based on information of lattice orientation. The direction of a lattice plane can be represented by a point through projection of the direction on to the stereographic polar net (Kocks et al. 1998). Textures affect the property of materials and are usually induced during processing. In OIM, the misorientation angle can be statistically analyzed as shown in *Figure 12*, which compares the changes of {001} direction misorientation angle distribution with and without LSP for copper (*Figure 12a*) and nickel (*Figure 12b*), respectively. The misorientation angle is relative to the surface normal of the sample. The angle distribution curves for both nickel and copper in *Figure 12* show very low intensities at low angles before LSP. The reason is that for face-centered cubic (FCC) metals such as nickel and copper there are three perpendicular {001} pole directions for each grain. Even if one pole is low angle (close to surface-normal direction), the other two poles are high angles. The sample as received has slight textures, which rotate the lattice and make the low angle intensity even smaller. Texture variations of copper and nickel after LSP share a common feature, that is, trending toward the ideal {001} direction (low angle). Especially for angles less than 10 degrees, both copper and nickel show an obvious intensity increase after LSP. A striking difference between nickel and copper is that the {001} texture of nickel has a sharper density increase at small angles.

The difference in {001} texture change of copper and nickel can be explained after examining the inverse pole figures in *Figure 13*, which gives complete information on the variations of the lattice orientations. After LSP of copper, the {111} texture intensity is weakened, while the {101} and {001} textures intensities are enhanced. After LSP of nickel, {111} texture intensity is weakened, {001} texture is enhanced, but the {101} texture does not change much. After LSP, the {001} texture of nickel is stronger than copper.

Both nickel and copper are FCC metals, and the major slip system is {111} lattice plane along [110] lattice direction, and the {100}[110] and {101}[110] slip systems are also possible (Hirth and Lothe 1982). Nickel, however, is stronger and less ductile than cooper. In LSP, the major deformation direction is downward along the surface-normal direction. The dynamic downward stress equals the shock pressure (*Figure 3*) and is much higher than the energy needed for plastic deformation. As a result, the misorientation angle distributions of copper and nickel both show density increases along {001} direction after LSP (*Figure 12*). The downward deformation also favors {101} texture density increase because the shear stress is largest at 45 degrees to the surface normal. The possible slip systems of FCC metals also favor {101} texture formations. The initial density of {111} texture is weakened with the density increase of other textures.

Texture change relates to the rotation of lattice orientation to the preferred directions. The lattice orientation rotation in LSP is realized through the high

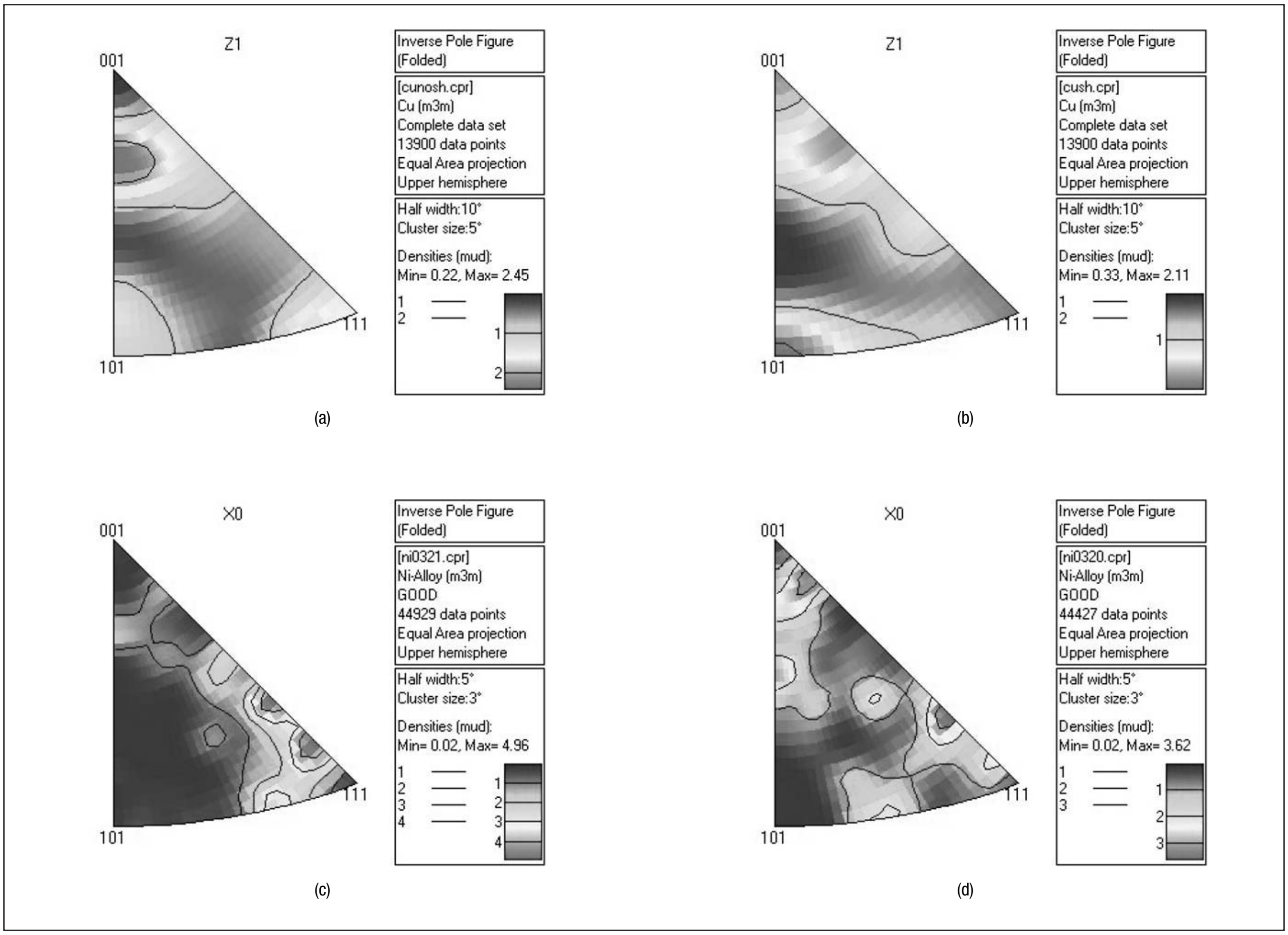

(a) (b) (c) (d)

Figure 13
Inverse Pole Figure Comparisons. (a) Copper, without LSP. (b) Copper, with LSP. (c) Nickel, without LSP. (d) Nickel, with LSP. "M.U.D." is abbreviation for Multiple of Uniform (average) Density

strain rate plastic deformations. Plastic deformation is a result of subgrain structure (low-angle grain boundaries or dislocation) formation and multiplication, twinning, and stacking fault formation. The energy required for subgrain formation is proportional to Gb^2, where G is the shear modulus and b is the Burger's vector. For FCC metals, $b = 0.3536a_0$, where a_0 is the lattice constant. The lattice constant of copper is 0.361 nm, and 0.352 nm for nickel. But the shear modulus of nickel is 73 GPa, 1.74 times that of copper. Thus, the energy of dislocation formation of nickel is 1.65 times that of copper. Nickel experiences larger resistance in changing its lattice orientations than copper does. At the same time, the shear stress is substantially lower than the normal stress. For these reasons, copper shows more significant density increase in {101} texture, while nickel shows much less. This also explains the sharper density increase of low angle {001} of nickel than copper (*Figure 12*), because the density increase of nickel in {101} is limited and the {101} texture dissipates more deforming energy in copper than that in nickel. In general, the textures for both nickel and copper before and after LSP are not strong.

Subgrain structures. Subgrain structures can be quantitatively analyzed through OIM measurements because OIM is based on submicron spatial accuracy data acquisition of misorientation angles, and the misorientation angle accuracy is less than one degree. *Figures 14a* and *14b* show the microstructures of copper without and with LSP, respectively. *Figures 14c* and *14d* show the microstructures of nickel without and with LSP, respectively. Grain boundaries are shown in thick black lines. The thin black lines show subgrain boundaries whose misorientation angles are larger than 1.5 degrees. The red

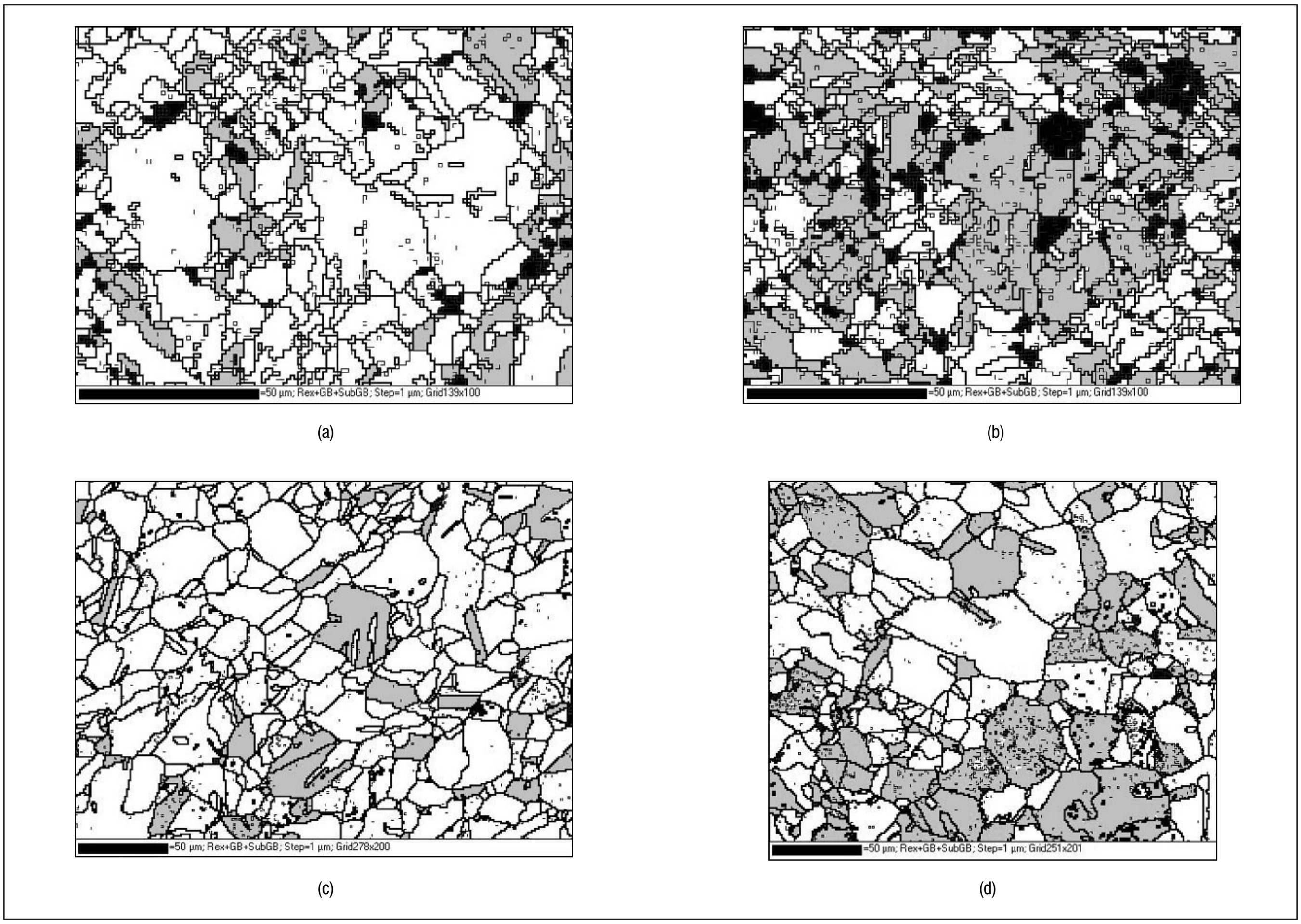

(a) (b) (c) (d)

Figure 14
Subgrain Structure Changes Through LSP. (a) Copper, no LSP. (b) Copper, with LSP. (c) Nickel, no LSP. (d) Nickel, with LSP. Red color: highly deformed region, Silver color: grain with substructures, White color: grain fully recrystallized, Thick black lines: grain boundaries with misorientation angle larger than 10 degrees, Thin black lines: subgrain boundaries with misorientation angle larger than 1.5 degrees.

grains are highly deformed grains, silver colored grains are grains with substantial substructures such as twins and dislocations, and the white colored grains are fully recrystallized grains that have less defects and substructures. It is observed that copper has a larger increase in substructure and in highly deformed region after LSP than nickel, while both show substantial increase in substructure and highly deformed regions with LSP compared with that without LSP. *Table 2* gives a quantitative comparison.

The substructures in OIM are, in fact, dislocations on the top surface of the sample. The substructures change due to LSP is featured by high speed and high uniformity compared with normal deformation processes such as cold rolling. Shock front serves as subgrain structure (dislocation) sources when the shock pressure is higher than the critical shear stress. According to Meyer and Murr (1981), dislocations are homogeneously nucleated at (or close to) the shock front by the deviatoric stresses set up by the shock load; the generation of these dislocations relaxes the deviatoric stresses. These dislocations

Table 2
Microstructure Changes of Copper and Nickel After LSP

% of Area	Cu, without LSP	Cu, with LSP	Ni, without LSP	Ni, with LSP
With substructures	11±2.1%	46.3±2.5%	13±2.0%	39.4±1.8%
Highly deformed	4.4±0.9%	11±1.3%	0.5±0.5%	4.2±0.7%
Fully recrystallized	82.6±3.0%	42.7±3.2%	86.5±2.9%	56.4±2.5%

move short distances at subsonic speeds, and new dislocation interfaces are generated as the shock wave propagates through the material. The critical shear stress of nickel is about 65% higher than copper because the critical shear stress is proportional to the dislocation energy. Under the same shock load, substructures in copper have a longer time to develop and develop faster than in nickel. When shock pressure becomes less than the critical stress, substructure and plastic deformation growth halts. Hardness and strength are macroscopic measures of plastic deformation. Nickel has higher hardness and strength than copper. The discussion in section 3 also helps explain the changes in microstructure. Referring to the Hugniot curve (*Figure 2a*), one sees that the increase of normalized density of nickel is 20% less than that of copper with the increase of shock pressure. All these lead to the conclusion that substructures in nickel are more difficult to develop than in copper under the same LSP conditions.

The substantial increase of substructures is the major cause of strength and hardness improvement in LSP. With the increase of substructures, the subgrain size decreases, which has an effect similar to grain refinement. According to Murr (1981), the flow stress

$$\sigma = \sigma_0 + k_1 D^{-1/2} + k_2 d^{-1} \qquad (14)$$

where σ_0, k_1, and k_2 are material constants, D is grain size, and d is subgrain size. As a result, the yield strengths of copper and nickel increase after LSP. Both the compressive surface residual stress and the refined microstructure in LSP contribute to the fatigue life improvement.

Conclusions

For microscale LSP, a new shock pressure model taking into account mass, energy, and momentum conservation was formulated with plasma modeled as laser-supported combustion wave and its spatial expansion effects accounted for. The new model provides better correlation with experimental results in terms of deformation. Stress and strain analysis was extended to 3D and considered finite geometry, which again is important for microscale LSP. Tests showed microscale LSP more than doubled the fatigue life of copper and nickel specimens under the test condition. OIM measurements quantitatively showed LSP improved grain size uniformity and slightly increased texture. Increase of subgrain structures was also quantified and used to help explain the fatigue performance improvement by LSP. The differences between copper and nickel were explained in terms of their properties and response to shock waves.

Acknowledgments

Financial support from the National Science Foundation under grant DMI-9813453 and equipment support from ESI are gratefully acknowledged. Assistance with SEM/OIM measurements rendered by Dr. Alex Limanov is also appreciated.

References

Assay, J.R. and Shahinpoor, M. (1992). *High-Pressure Shock Compression of Solids.* New York: Springer-Verlag, pp78-82.

Berthe, L. et al. (1998). “Experimental study of the transmission of breakdown plasma generated during laser shock processing.” *European Physical Journal of Applied Physics* (v3), pp215-218.

Clauer, A.H. et al. (1981). “Effects of laser induced shock waves on metals.” *Shock Waves and High Strain Phenomena in Metals—Concepts and Applications.* New York: Plenum, pp675-702.

Fabbro, R. et al. (1990). “Physical study of laser-produced plasma in confined geometry.” *Journal of Applied Physics* (v68, n2, July 1990), pp775-784.

Hirth, J.P. and Lothe, J. (1982). *Theory of Dislocations,* 2nd ed. New York: John Wiley & Sons, pp182-274.

Kocks, U.F. et al. (1998). *Texture and Anisotropy.* Cambridge, UK: Cambridge Univ. Press, pp44-100.

Meyers, M.A. and Murr, L.E. (1981). *Shock Waves and High Strain Rate Phenomena in Metals—Concepts and Applications.* New York: Plenum Press, pp487-530, 1048.

Murr, L.E. (1981). “Residual microstructure—Mechanical property relations in shock-loaded metals and alloys.” *Shock Waves and High Strain Phenomena in Metals—Concepts and Applications.* New York: Plenum, pp635-655.

Novikov, V. (1997). *Grain Growth and Control of Microstructure and Texture in Polycrystalline Materials.* New York: CRC Press, p11.

Peyre, P. et al. (1995). “Laser induced shock waves as surface treatment for 7075-T7351 aluminum alloy.” *Surface Engg.* (v11), pp47-52.

Pirri, A.N. et al. (1978). “Plasma energy transfer to metal surfaces irradiated by pulsed lasers.” *AIAA Journal* (v16, n12), pp1296-1304.

Root, R.G. (1989). “Modeling of post-breakdown phenomena.” *Laser Induced Plasmas and Application.* New York: Marcel Dekker, Inc., pp95-99.

Simons, G.A. (1984). “Momentum transfer to a surface when irradiated by a high-power laser.” *AIAA Journal* (v22, n9), pp1275-1280.

Vogel, A. et al. (1996). “Plasma formation in water by picosecond and nanosecond Nd:YAG laser pulses.” *IEEE Journal of Selected Topics in Quantum Electronics* (v2, n4, Dec. 1996), pp847-871.

Zhang, W. and Yao, Y.L. (2000a). “Improvement of laser induced residual stress distributions via shock waves.” ICALEO’2000, Laser Material Processing (v89), ppE183-E192.

Zhang, W. and Yao, Y.L. (2000b). “Micro scale laser shock processing of metallic components.” *ASME Journal of Mfg. Science and Engg.* (submitted).

Zhang, H. and Yu, C. (1998). “Laser shock processing of 2024-T62 aluminum alloy.” *Materials Science and Engg. A* (v257), pp322-327.

Authors’ Biographies

Wenwu Zhang has a PhD from Columbia University and is currently with GE. Y. Lawrence Yao is an associate professor in the Dept. of Mechanical Engineering at Columbia University, where Yao also directs the manufacturing engineering program. Yao has a PhD from the University of Wisconsin-Madison.